

A systematic *Chandra* study of Sgr A*: II. X-ray flare statistics

Qiang Yuan,^{1,2★} Q. Daniel Wang,^{3★} Siming Liu^{1,2} and Kinwah Wu⁴

¹Key Laboratory of Dark Matter and Space Astronomy, Purple Mountain Observatory, Chinese Academy of Sciences, Nanjing 210008, China

²School of Astronomy and Space Science, University of Science and Technology of China, Hefei 230026, China

³Department of Astronomy, University of Massachusetts, 710 North Pleasant St., Amherst, MA 01003, USA

⁴Mullard Space Science Laboratory, University College London, Holmbury St. Mary, Dorking, Surrey, RH5 6NT, UK

Accepted 2017 September 14. Received 2017 September 14; in original form 2017 July 25

ABSTRACT

The routinely flaring events from Sgr A* trace dynamic, high-energy processes in the immediate vicinity of the supermassive black hole. We statistically study temporal and spectral properties, as well as fluence and duration distributions, of the flares detected by the *Chandra* X-ray Observatory from 1999 to 2012. The detection incompleteness and bias are carefully accounted for in determining these distributions. We find that the fluence distribution can be well characterized by a power law with a slope of $1.73^{+0.20}_{-0.19}$, while the durations (τ in seconds) by a lognormal function with a mean $\log(\tau) = 3.39^{+0.27}_{-0.24}$ and an intrinsic dispersion $\sigma = 0.28^{+0.08}_{-0.06}$. No significant correlation between the fluence and duration is detected. The apparent positive correlation, as reported previously, is mainly due to the detection bias (i.e. weak flares can be detected only when their durations are short). These results indicate that the simple self-organized criticality model has difficulties in explaining these flares. We further find that bright flares usually have asymmetric light curves with no statistically evident difference/preference between the rising and decaying phases in terms of their spectral/timing properties. Our spectral analysis shows that although a power-law model with a photon index of 2.0 ± 0.4 gives a satisfactory fit to the joint spectra of strong and weak flares, there is weak evidence for a softer spectrum of weaker flares. This work demonstrates the potential to use statistical properties of X-ray flares to probe their trigger and emission mechanisms, as well as the radiation propagation around the black hole.

Key words: accretion, accretion discs – methods: data analysis – Galaxy: centre – X-rays: individual (Sgr A*).

1 INTRODUCTION

Low-luminosity supermassive black holes (LL-SMBHs) represent the silent majority (~ 90 per cent) of SMBHs in our Universe. Sgr A* is in a rather steady low-luminosity state, referred to as the ‘quiescent state’, with peak emission in the sub-millimeter band. Occasionally, there are substantial variations in the emission, known as flares, which are most prominent in the (near) infrared (NIR/IR) and X-ray bands (Baganoff et al. 2001; Genzel et al. 2003). The spatial, spectral and temporal decompositions of the X-ray emission of Sgr A* show that 1) the quiescent emission is mostly extended and the flaring emission is point-like (Baganoff et al. 2003; Wang et al. 2013); 2) there is an additional point-like, super-soft quiescent component which is not accounted for by detected flares (Roberts et al. 2017); 3) the spectrum is optically thin thermal for the quiescent extended emission while featureless power laws for flares

(Baganoff et al. 2001; Nowak et al. 2012; Wang et al. 2013); 4) the rate of X-ray flares is about 1 \sim 2 per day (Ponti et al. 2015; Yuan & Wang 2016) or about 3 per day after correcting for the detection threshold (Mossoux & Grosso 2017), which is a factor of a few smaller than that of NIR/IR ones (Eckart et al. 2006).

The quiescent emission of Sgr A* can be explained in terms of the radiatively inefficient inflow/outflow model (Yuan, Quataert & Narayan 2003; Narayan et al. 2012; Wang et al. 2013; Yuan et al. 2015; Roberts et al. 2017). The origin of the flares is, however, still unclear. From the temporal spectral properties, crucial information regarding the radiative mechanisms associated with the flares can be extracted. However, existing studies tended to focus on individual strong flares detected with reasonably good counting statistics, mostly via observations made with *XMM-Newton* (Porquet et al. 2003; Bélanger et al. 2005; Yusef-Zadeh et al. 2006; Porquet et al. 2008) and a few with *Chandra* (Baganoff et al. 2001; Nowak et al. 2012) and *NuSTAR* (Barrière et al. 2014; Pontiet et al. 2017). Only a few works studied the flare population, with limited flare samples (Nielsen et al. 2013; Zhang et al. 2017).

* E-mail: yuanq@pmo.ac.cn (QY); wqd@astro.umass.edu (QDW)

Table 1. Properties of the ACIS-I flares used for spectral analysis.

Flare ID	$\log(F/\text{cts})$	$\log(\tau/\text{ks})$	t_{start} (ks)	t_{end} (ks)	$F_{\text{pile-up}}$
11	1.07 ± 0.23	0.45 ± 0.20	54 270.053	54 274.283	1.00
12	1.35 ± 0.12	0.03 ± 0.12	89 000.851	89 002.455	0.93
13	1.00 ± 0.26	0.14 ± 0.29	130 520.43	130 522.51	1.00
14	0.82 ± 0.30	-0.04 ± 0.41	133 277.53	133 278.89	1.00
15	1.85 ± 0.10	0.80 ± 0.09	138 651.24	138 659.31	1.00
16	1.72 ± 0.09	0.60 ± 0.11	138 771.38	138 777.35	0.98
17	1.02 ± 0.19	0.01 ± 0.26	138 781.96	138 783.49	1.00
18	1.49 ± 0.12	0.64 ± 0.14	138 805.22	138 811.78	1.00
19	1.39 ± 0.12	0.18 ± 0.09	138 864.21	138 866.47	0.95
110	1.09 ± 0.18	0.23 ± 0.21	138 877.64	138 880.18	1.00
111	2.18 ± 0.07	0.76 ± 0.10	139 036.87	139 044.73	0.92
112	0.94 ± 0.24	-0.14 ± 0.61	139 464.54	139 465.62	1.00
113	1.17 ± 0.22	0.47 ± 0.24	172 451.56	172 455.98	1.00
114	0.92 ± 0.21	-0.20 ± 0.28	205 542.87	205 543.81	0.99
115	1.77 ± 0.08	0.83 ± 0.09	239 074.25	239 084.39	1.00
116	1.15 ± 0.17	0.30 ± 0.21	265 566.39	265 569.39	1.00
117	1.07 ± 0.19	0.32 ± 0.16	275 579.64	275 582.78	1.00
118	1.14 ± 0.15	0.30 ± 0.16	305 152.20	305 155.20	1.00
119	0.99 ± 0.26	-0.49 ± 0.51	326 370.81	326 371.29	0.91
120	1.14 ± 0.21	0.51 ± 0.26	333 497.06	333 501.92	1.00
121	1.21 ± 0.18	0.36 ± 0.26	333 503.03	333 506.47	1.00
122	1.78 ± 0.12	0.55 ± 0.19	359 001.19	359 005.59	0.95
123	1.90 ± 0.12	0.61 ± 0.09	359 026.86	359 032.09	0.94
124	1.28 ± 0.14	0.39 ± 0.13	417 781.80	417 785.48	1.00

Note. Columns from left to right are: flare ID, logarithmic flare fluence, logarithmic flare duration, start and end times from UT 1998-01-01 00:00:00, which define the flare intervals, and pile-up correction factor.

Moreover, the spectral shape of such flares is often modelled by an absorbed power law. A comparison among the photon indices (Γ) obtained for various flares is therefore not straightforward, when Γ is strongly correlated with the foreground absorption column density N_{H} in the spectral fits. There could be differences in the modelling of such details due to adoption of different versions of the absorption cross-sections, dust absorption/scattering and/or metal abundance pattern. For bright flares detected by *Chandra*, pile-up effects, which include the grade migration (Davis 2001), can be problematic, as they cause distortion in the spectra data. Whether or not, and/or how the pile-up is treated can therefore affect the values of the photon indices when fitting the spectral data. With these in consideration, one finds that essentially all flares can be consistently characterized with a power law of $\Gamma \simeq 2$ and $N_{\text{H}} \simeq 1.5 \times 10^{23} \text{ cm}^{-2}$ of neutral material (Porquet et al. 2008; Nowak et al. 2012). This column density would be slightly smaller when dust scattering is accounted for separately. Nevertheless, the studies of *NuSTAR* flares which extended the spectral coverage beyond 10 keV (up to about 70 keV; Barrière et al. 2014) and *Swift* ones (Degenaar et al. 2013) do sometimes show that they may have different photon indices (e.g. $\Gamma \sim 3$). In this work, we extend the spectral analysis to relatively faint flares by both measuring hardness ratios (HRs) of individual flares and fitting to stacked data.

Flare statistics, on the other hand, may provide insights into the driving mechanism and how flares are triggered. It has been argued that flares are associated with the ejection of plasma blobs triggered by magnetic reconnection (e.g. Yusef-Zadeh et al. 2006). One of the magnetic reconnection scenarios is that the system shows characteristics of self-organized criticality (SOC). In it, a critical state is reached gradually by a non-linear energy build-up, followed by an avalanche energy release, which manifests as a flaring event (e.g. Katz 1986; Bak, Tang & Wiesenfeld 1987). In such an SOC flaring

model, if the system is scale-free, the total energy released in the flare, the peak rate of energy dissipation and the flaring time duration should all obey a power-law distribution, and the slopes of these three power laws are determined by the effective geometric dimension of the system (Aschwanden 2012; Aschwanden et al. 2016). SOC models have been applied to explain the statistics of flares in the Sun (e.g. Lu & Hamilton 1991; Aschwanden 2011) and in astrophysical black hole systems (Wang & Dai 2013; Li et al. 2015). The 3-Ms data of Sgr A* obtained in the *Chandra* X-ray Visionary Project (XVP) (Neilsen et al. 2013) have shown that the X-ray flaring statistics of the source are consistent with those predicted by SOC models with a spatial dimension $S = 3$ (Li et al. 2015; Wang et al. 2015). However, the analyses might be limited by a relatively small sample of flares with a narrow fluence range and by lacking a proper account for incompleteness and bias in the flare detection; the results obtained should be taken with caution.

Yuan & Wang (2016, hereafter Paper I) have presented a systematical search for X-ray flares in 84 *Chandra* observations of Sgr A*. 46 of these observations were taken before 2012, using the Advanced CCD Imaging Spectrometer–Imaging array (ACIS-I), while the other 38 in 2012, using the Advanced CCD Imaging Spectrometer–Spectroscopy array with the high-energy transmission gratings (ACIS-S/HETG0, where ‘0’ refers to the non-dispersed zeroth order). *Chandra* observations taken after 2012 are not included in the search because of the varying appearance of the X-ray bright magnetar, SGR J1745-2900 (Kennea et al. 2013), just 2.4 arcsec away from Sgr A*, which complicates the detection and statistical analysis of Sgr A* flares. With an improved unbinned likelihood method, the search finds a total of 82 flares in the ~ 4.5 Ms observations, about 1/3 of which are newly detected ones (see Tables 1 and 2 for a sub-sample with a relatively low pile-up effect). These two *Chandra* samples of Sgr A* flares form the base

Table 2. Properties of the ACIS-S/HETG0 flares used for spectral analysis.

Flare ID	$\log(F/\text{cts})$	$\log(\tau/\text{ks})$	t_{start} (ks)	t_{end} (ks)	$F_{\text{pile-up}}$
S1	1.94 ± 0.05	0.49 ± 0.05	453 264.94	453 269.58	0.93
S2	1.82 ± 0.11	0.30 ± 0.10	453 933.00	453 935.77	0.92
S3	1.85 ± 0.06	0.59 ± 0.05	459 317.44	459 323.28	0.95
S4	1.85 ± 0.09	0.94 ± 0.08	459 428.50	459 438.92	1.00
S5	2.09 ± 0.04	0.60 ± 0.03	460 110.73	460 116.71	0.92
S6	2.01 ± 0.08	0.51 ± 0.11	460 253.06	460 257.06	0.92
S7	2.24 ± 0.06	0.82 ± 0.10	467 370.02	467 380.57	0.93
S8	1.18 ± 0.13	0.27 ± 0.14	445 170.33	445 173.11	1.00
S9	1.37 ± 0.11	−0.10 ± 0.09	448 630.66	448 631.84	0.92
S10	1.38 ± 0.11	0.12 ± 0.10	448 633.82	448 635.80	0.95
S11	1.37 ± 0.11	0.19 ± 0.10	448 638.60	448 640.92	0.96
S12	1.55 ± 0.08	0.59 ± 0.08	452 260.13	452 265.97	1.00
S13	1.43 ± 0.11	0.40 ± 0.14	452 746.05	452 749.81	1.00
S14	1.36 ± 0.11	0.67 ± 0.13	452 774.14	452 781.16	1.00
S15	1.41 ± 0.18	0.86 ± 0.58	453 136.68	453 143.17	1.00
S16	1.27 ± 0.12	0.47 ± 0.13	453 168.52	453 172.94	1.00
S17	1.10 ± 0.21	0.64 ± 0.32	453 192.47	453 199.03	1.00
S18	1.00 ± 0.18	0.32 ± 0.19	453 821.66	453 824.80	1.00
S19	1.11 ± 0.15	0.20 ± 0.15	453 937.72	453 940.09	1.00
S20	1.06 ± 0.17	0.47 ± 0.15	453 944.22	453 948.64	1.00
S21	1.56 ± 0.08	0.74 ± 0.07	459 039.34	459 047.59	1.00
S22	1.16 ± 0.14	0.43 ± 0.12	459 057.69	459 061.73	1.00
S23	1.39 ± 0.11	0.09 ± 0.14	459 176.29	459 178.13	0.94
S24	1.03 ± 0.15	−0.09 ± 0.14	459 217.17	459 218.39	0.99
S25	1.36 ± 0.11	0.02 ± 0.10	459 380.52	459 382.10	0.94
S26	1.47 ± 0.09	0.04 ± 0.08	459 508.28	459 509.93	0.93
S27	0.95 ± 0.18	−0.29 ± 0.19	459 605.82	459 606.58	0.95
S28	1.27 ± 0.13	0.55 ± 0.14	459 860.71	459 866.03	1.00
S29	0.96 ± 0.28	0.55 ± 0.33	459 873.61	459 878.93	1.00
S30	1.41 ± 0.10	0.73 ± 0.09	460 040.91	460 048.97	1.00
S31	0.86 ± 0.20	−0.05 ± 0.23	460 268.82	460 270.16	0.99
S32	1.60 ± 0.08	0.13 ± 0.05	460 452.53	460 454.55	0.92
S33	1.57 ± 0.10	1.24 ± 0.09	460 482.85	460 508.95	1.00
S34	1.37 ± 0.10	0.52 ± 0.13	460 539.33	460 544.29	1.00
S35	1.30 ± 0.12	0.40 ± 0.13	460 781.60	460 785.36	1.00
S36	1.22 ± 0.15	0.54 ± 0.17	465 968.67	465 973.87	1.00
S37	1.40 ± 0.10	0.38 ± 0.09	466 057.06	466 060.66	1.00
S38	0.74 ± 0.24	−0.14 ± 0.25	466 827.00	466 828.08	1.00
S39	1.20 ± 0.13	0.34 ± 0.19	466 970.77	466 974.05	1.00
S40	1.19 ± 0.24	0.88 ± 0.34	467 413.12	467 424.50	1.00
S41	1.59 ± 0.12	0.38 ± 0.10	467 529.97	467 533.23	0.96
S42	1.66 ± 0.08	0.84 ± 0.10	467 965.49	467 975.87	1.00
S43	0.83 ± 0.19	−0.03 ± 0.19	468 004.79	468 006.19	1.00
S44	1.49 ± 0.10	0.51 ± 0.14	468 076.64	468 081.50	1.00

Note. Same as Table 1. The central horizontal line separates the strong flares from the weak ones.

for the statistical analysis presented here. In addition, the detection incompleteness, uncertainty and bias are carefully studied for the first time, which is especially important for a statistical analysis including weak flares close to the detection threshold, as is the case for the work reported here. We adopt the detection response matrices, as obtained in Paper I, to better characterize the detection effects on the flare statistics.

To provide further constraints on the nature of the flares, we statistically characterize their time profiles and spectral variations. There have been a few studies on such properties of a few individual bright flares (e.g. Baganoff et al. 2001; Porquet et al. 2003; Bélanger et al. 2005; Yusef-Zadeh et al. 2006; Porquet et al. 2008; Nowak et al. 2012; Degenaar et al. 2013; Barrière et al. 2014; Ponti et al. 2017). We extend these studies to relatively weak flares, e.g. via stacking analysis.

The organization for the rest of this paper is as follows. In Section 2, we present the statistical analysis of the X-ray flares. The implications of our results in understanding the nature of the flares are briefly discussed in Section 3. Finally, we summarize our work in Section 4.

2 FLARE STATISTICS

2.1 Fluence and duration distributions

This analysis follows the approach of Li et al. (2015) to characterize the probability distributions of the flare fluence (F) and duration (τ). The distribution of F is assumed to be a power law, $P(F) = A \cdot F^{-\alpha}$, while τ follows a lognormal function, $N(\log \tau; \mu, \sigma)$, in which $\mu = \log(B \cdot F^\beta)$ is the expected mean correlation with the fluence

Table 3. The best-fit, posterior mean values and the 95 per cent limits of the logarithmic normalization ($\log A$) and power-law index (α) of the fluence distribution, and the logarithmic normalization ($\log B$), power-law index (β) and dispersion width (σ) of the fluence–duration correlation (see Section 2.1).

	$\log A$		α		$\log B$		β		σ	
	Best	Posterior mean and 95 per cent limits	Best	Posterior mean and 95 per cent limits	Best	Posterior mean and 95 per cent limits	Best	Posterior mean and 95 per cent limits	Best	Posterior mean and 95 per cent limits
ACIS-I	2.13	$2.26^{+0.56}_{-0.55}$	1.68	$1.77^{+0.33}_{-0.32}$	3.34	$3.38^{+0.46}_{-0.38}$	0.09	$0.08^{+0.21}_{-0.23}$	0.25	$0.28^{+0.15}_{-0.09}$
ACIS-S/HETG0	2.24	$2.29^{+0.46}_{-0.40}$	1.71	$1.75^{+0.28}_{-0.24}$	3.35	$3.45^{+0.53}_{-0.41}$	0.10	$0.05^{+0.26}_{-0.30}$	0.28	$0.32^{+0.13}_{-0.09}$
Joint fit	2.22	2.23 ± 0.29	1.72	$1.73^{+0.20}_{-0.19}$	3.38	$3.39^{+0.27}_{-0.24}$	0.09	$0.08^{+0.15}_{-0.17}$	0.28	$0.28^{+0.08}_{-0.06}$

and σ is the Gaussian width of $\log \tau$.¹ Hereafter, we use $\log F$ and $\log \tau$ as variables. The joint *intrinsic* probability distribution of the fluence ($\log F_i$) and duration ($\log \tau_i$) is then

$$\begin{aligned}
 P(\log F_i, \log \tau_i) &= P(\log F_i) \cdot P(\log \tau_i | \log F_i) \\
 &= F_i \cdot \ln 10 \cdot P(F_i) \cdot N(\log \tau_i; \log B + \beta \log F_i, \sigma). \quad (1)
 \end{aligned}$$

The joint probability distribution of the *detected* fluence ($\log F_d$) and duration ($\log \tau_d$) is

$$\begin{aligned}
 P(\log F_d, \log \tau_d) &= P(\log F_d, \log \tau_d; \log F_i, \log \tau_i) \\
 &\quad \otimes P(\log F_i, \log \tau_i), \quad (2)
 \end{aligned}$$

where \otimes means the convolution of $P(\log F_i, \log \tau_i)$ with $P(\log F_d, \log \tau_d; \log F_i, \log \tau_i)$, which is a redistribution matrix. It is obtained through Monte Carlo simulations for the two flare samples separately, accounting for the counting statistics and background-dependent detection incompleteness and bias (see Paper I). Individual flares are considered to be independent Poisson realizations. The logarithmic likelihood function of our N_d detected flare is then (Cash 1979)

$$\ln \mathcal{L}(\vec{\theta} | \text{Data}) = \sum_k^{N_d} \ln P(\log F_d^k, \log \tau_d^k) - N_{\text{pred}}, \quad (3)$$

where $\vec{\theta} = (A, \alpha, B, \beta, \sigma)$ represent the model parameters, the sum is over all the detections ($k = 1, \dots, N_d$) and

$$N_{\text{pred}} = \iint P(\log F_d, \log \tau_d) d \log F_d d \log \tau_d \quad (4)$$

is the expected total number of flares. We use the Markov Chain Monte Carlo (MCMC) method to maximize equation (3) and constrain the model parameters $\vec{\theta}$. Compared with Paper I, we improve the flare statistical study through proper considerations of the Poisson fluctuation and the detection bias in a joint fit of the fluence distribution and the fluence–duration correlation.

Table 3 gives the best-fit and posterior two-sided 95 per cent confidence ranges of the parameters. The corresponding one-dimensional and two-dimensional distributions of the fitting parameters are shown in Fig. 1. The parameters obtained for the ACIS-I and -S/HETG0 flares are consistent with each other.

The top two panels of Fig. 2 show the detection probability distribution as a function of $\log F_d$ and $\log \tau_d$ (equation 2) for the best-fitting models of the two flare samples, respectively. As a comparison, we show in the bottom two panels the intrinsic probability distribution without the convolution with the detection redistribution matrix. It clearly shows how an apparent correlation can be

obtained from an intrinsically nearly uncorrelated distribution between the fluence and duration. The detection redistribution matrix makes long duration, weak flares undetectable and the probability distribution wider.

We assess the goodness of the fit to the detected flares from each of the two detected flare samples via bootstrapping sampling. Fig. 3 presents the distributions of $C \equiv -2 \ln \mathcal{L}$ from the fits to the 1000 sets of bootstrapped flares, which are randomly realized from the best-fitting model. The number fraction with C smaller than that of the actual data ($C_{\text{best}} = -206.7$) is 72 per cent for the ACIS-S/HETG0 flares, suggesting that the data are well described by the model. The corresponding fraction is 95.1 per cent for the ACIS-I data, which means a slightly worse fitting.

We further jointly fit the two flare samples to improve the constraints on the model parameters. Since the effective area (exposure time) of the ACIS-I observations is on average a factor of ~ 2.6 (2.0) larger (smaller) than that of the ACIS-S/HETG0 observations (Paper I), we expect to have $P(F_i) = P(F_s) \cdot dF_s/dF_i \cdot t_i/t_s$, and hence $A_i = A_s \cdot 2.6^{\alpha-1}/2$, where the subscript ‘ i ’ (‘ s ’) stands for the ACIS-I (-S/HETG0) flares. Similarly, for the fluence–duration correlation we have $B_i = B_s/2.6^\beta$. The joint fit significantly tightens the constraints on the model parameters, which are included in Table 3.

The power-law index of the fluence distribution, $\alpha \sim 1.7$, is consistent with those found in Neilsen et al. (2013) and Li et al. (2015). But we find little intrinsic correlation between the fluence and duration ($\beta \sim 0$), although an apparent correlation is present for the detected flares (e.g. Fig. 1; Paper I; Neilsen et al. 2013; Li et al. 2015). Such correlations are largely due to the detection bias and uncertainty, which were not fully accounted for previously.

2.2 Flare time profiles

We characterize the asymmetry properties of flare time profiles. In Paper I, we used only the standard symmetric Gaussian profiles to approximate the flare light curves. Here, we relax this approximation for those ‘strong’ flares, each with fluence $F > 50$ counts. We adopt a modified Gaussian function of varying width (Stancik & Brauns 2008)

$$\sigma(t) = \frac{2\sigma_0}{1 + \exp[-\xi(t - t_0)]}. \quad (5)$$

This function recovers to the standard Gaussian function with a constant width σ_0 when $\xi = 0$. When $\xi > 0$, the profile will be broader for $t > t_0$ and narrower for $t < t_0$, and vice versa when $\xi < 0$.

We refit the light curves of the strong flares, using the function to derive the shape asymmetry parameter ξ . For consistency, the single function is applied in all fits, including those with indications for subflares, because their effects are generally too subtle to be

¹ This treatment is essentially the same as adding an ‘intrinsic’ error to the statistical one of $\log \tau$, as done in Paper I.

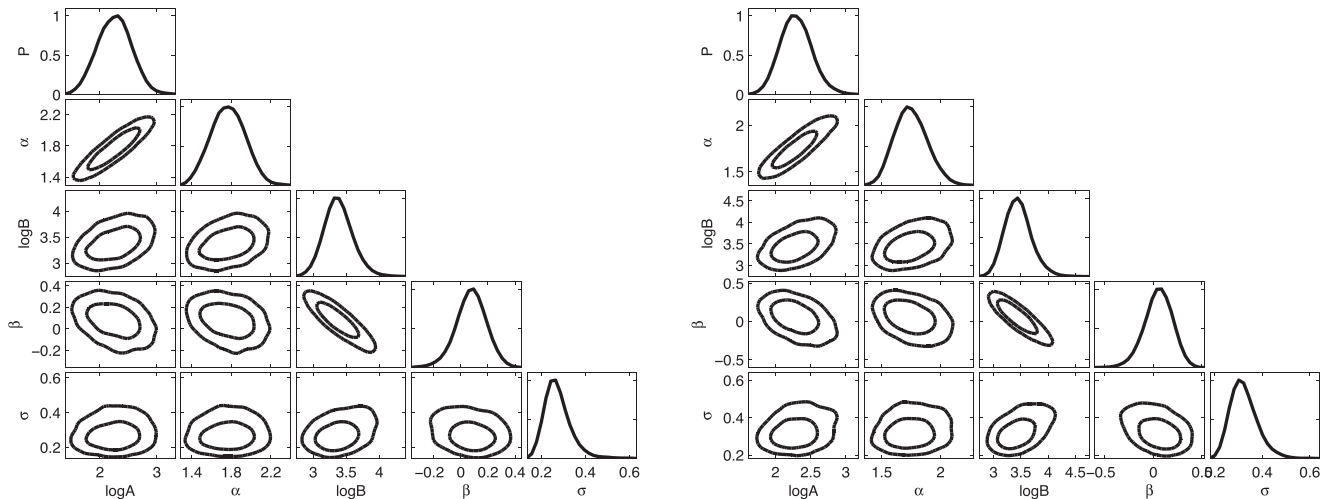


Figure 1. Fitting 1D (diagonal) probability distributions and 2D (off-diagonal) contours at 68 and 95 per cent confidence levels of the model parameters, ($\log A$, α , $\log B$, β , σ), for the ACIS-I (left) and -S/HETG0 (right) data.

effectively distinguished from those arising from the overall profile asymmetry. The results are shown in Fig. 4, suggesting that about half of the flares have positive ξ values (hence fast rise and slow decay) and the other half show negative ξ (slow rise and fast decay). The number of the flares with positive ξ is only slightly larger than that with negative ξ . There is no obvious trend of ξ with respect to the fluence. A general anticorrelation is present between ξ and the flare durations for both samples, although each has one exception, which has the shortest duration among the flares.

2.3 Flare spectral properties

To characterize the spectral properties of a flare, we first define its spectral hardness ratio (HR) as

$$\text{HR} = \frac{N_c(4 - 8 \text{ keV})}{N_c(2 - 4 \text{ keV})}, \quad (6)$$

where N_c is the number of net (quiescent contribution-subtracted) counts accumulated within a $\pm 3\sigma$ range of the Gaussian light curve. The event rate of the quiescent contribution below (above) 4 keV is calculated using the events detected over non-flaring time windows, which is 2.33 (2.55) cts/ks for the ACIS-I data and 0.73 (1.14) cts/ks for the -S/HETG0 data. Furthermore, to characterize the spectral evolution of a flare, we separate the counts into two parts, the rising phase before the best-fitting Gaussian peak and the decaying phase after the peak. The results are given in Fig. 5.

We adopt a linear function, $\text{HR} = \lambda \cdot \log F + \eta$ ($\text{HR} = \mu \cdot \log P + \nu$), to characterize the correlation between the HR and logarithmic fluence F (peak rate P) for the two flare samples. The fitting results are given in Tables 4 and 5. For the ACIS-I flares, a positive correlation is seen for both the rising (at a confidence level of $2\sigma \sim 3\sigma$) and decaying phases ($\sim 4\sigma$). For the ACIS-S/HETG0 flares, however, this correlation is less significant. Only for the rising phase, we find a marginal correlation with a significance of $\sim 2.4\sigma$ (1.2σ) for the HR–fluence (HR–peak rate) correlation. The ACIS-I data suggest that brighter flares tend to have harder spectra than weaker ones, especially for the decaying phase. This trend is, however, not obvious for the ACIS-S/HETG0 flares.

We next focus on the mean spectral properties of relative faint flares, based on the analysis of their accumulated spectra. We limit

our spectral analysis to those flares with negligible pile-up effects, which are estimated from the analysis of the light curves of individual flares in a forward fitting procedure (Paper I). In principle, correction may also be made in spectral fits, using the pile-up model (Davis 2001), as implemented in XSPEC. However, it is not clear how effective the correction may be for flares which vary strongly. In any case, the correction, including at least one more fitting parameter, would introduce additional uncertainties in the spectral parameter estimation (Nowak et al. 2012). Therefore, we select those flares with the pile-up correction factor greater than 0.9 (i.e. the pile-up effect is $\lesssim 10$ per cent).

We use an aperture radius of 1.5 arcsec to extract spectral data of Sgr A*. This extraction is made separately from the ACIS-I and -S/HETG0 observations. We extract on-flare spectral data from the time interval between the $\pm 3\sigma$ around the peak of each flare. If it contains subflares, then the interval is between their first -3σ and last $+3\sigma$. We add the spectral data of individual flares together to form an accumulated spectrum. To examine potential flux dependent properties, we form two separate ACIS-S spectra from 7 strong and 37 weak flares, according to their individual fluences, greater or less than $10^{1.8}$ counts (Table 2). The corresponding ACIS-I fluence criterion is $10^{2.2}$ counts, due to the larger effective area. We find that all our 24 selected ACIS-I flares have fluences below this criterion (Table 1) and all have pile-up correction factors < 0.9 . We further construct two off-flare spectra of Sgr A*, using the ACIS-I and -S/HETG0 data after excluding the time intervals of all the detected flares. These ‘quiescent’ spectra are exposure scaled and subtracted from the corresponding on-flare spectra in their analysis.

We fit the spectra with an absorbed power law. Specifically, the XSPEC model *tbabs* is used to model the foreground absorption, which includes the contribution from dust grain (Wilms et al. 2000), while *xscat* to account for the grain scattering (Smith, Valencic & Corrales 2016). The fitting is very insensitive to the location of the dust scattering. This parameter is thus fixed to 0.95 (i.e. close to Sgr A*). A test inclusion of the pile-up model shows that it has little effect on the best-fitting results, confirming our expectation.

The left-hand panel of Fig. 6 shows that the three spectra of the Sgr A* flares, i.e. the weak ACIS-I flares and the strong and weak ACIS-S ones, can be well fitted by a single absorbed power law

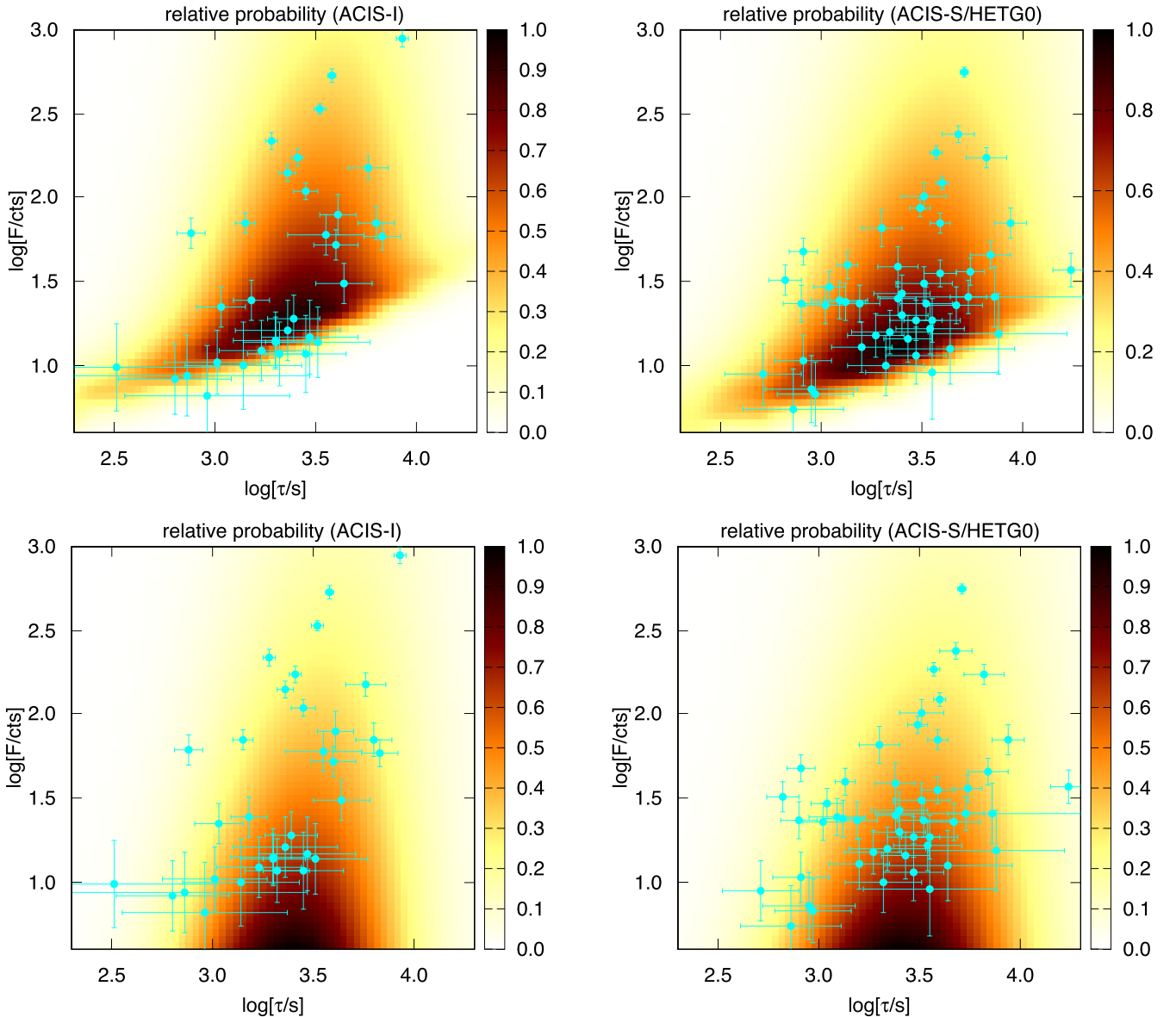


Figure 2. The images in the top two panels show the relative probability distributions of the flare detection as a function of the fluence and duration, for the ACIS-I (left) and -S/HETG0 (right) samples. The overlaid data points are from our detected flares in the respective samples (Paper I). For a comparison, the images in the bottom two panels show the intrinsic probability distributions of flares without convolution with the redistribution matrices.

($\chi^2/n.d.f. = 104/132$). The best-fitting photon index is 2.0 ± 0.4 and the absorption column density is $N_{\text{H}} = 13.5^{+3.1}_{-2.7} \times 10^{22} \text{ cm}^{-2}$. The uncertainties in these two parameters are largely due to their correlation, as shown in the right-hand panel of Fig. 6. To test any potential spectral dependence on the fluence of a flare, we first fix the column density to its best-fitting value (i.e. removing the above mentioned uncertainties) and then fit the photon index for the strong flare spectrum independently, while keeping the indices of the other two spectra jointly fitted. This fit does show a marginal evidence that the weak flares have a slightly larger average index than that of the strong ones (Fig. 7), which is consistent with the above HR analysis.

3 DISCUSSION

The above results provide new insights on understanding the nature of the X-ray flare emission of Sgr A* and their origins, as well as

indications for the possible relativistic and gravitational effects on the temporal and spectral properties of the flaring emission when propagating in the vicinity of the SMBH. We discuss these topics in the following.

3.1 Emission mechanism

We begin by a comparison of our spectral results with those obtained in previous studies, which are primarily focused on individual very bright flares. Ponti et al. (2017) showed that the average spectral index of three such flares observed by *XMM-Newton* is $\Gamma = 2.20 \pm 0.15$. Similar result was found for a sample of ten flares in a wider energy band of 1 – 79 keV by *NuSTAR* (Zhang et al. 2017). These results are slightly steeper than, but still consistent within the 68 per cent errors with that obtained here. There is an indication that strong flares tend to have harder spectra (Barrière et al. 2014; Zhang et al. 2017). See, however, Degenaar et al. (2013)

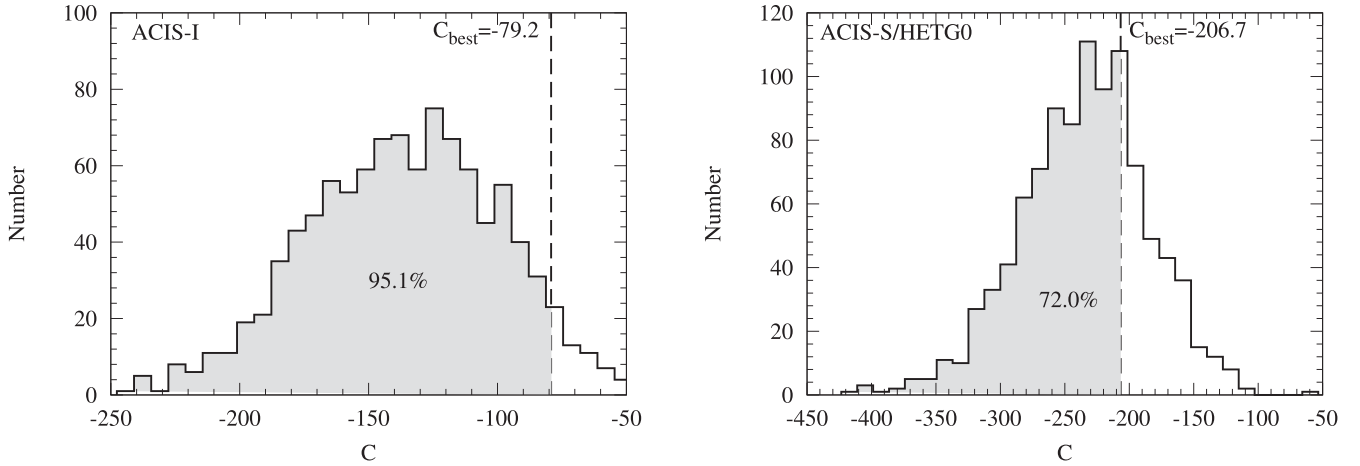


Figure 3. Distributions of the C -statistic values (defined as $-2 \ln \mathcal{L}$) of the fits to the 1000 sets of statistically realized flares, following the best-fitting fluence–duration distributions, for the ACIS-I (left) and -S/HETGO (right) samples.

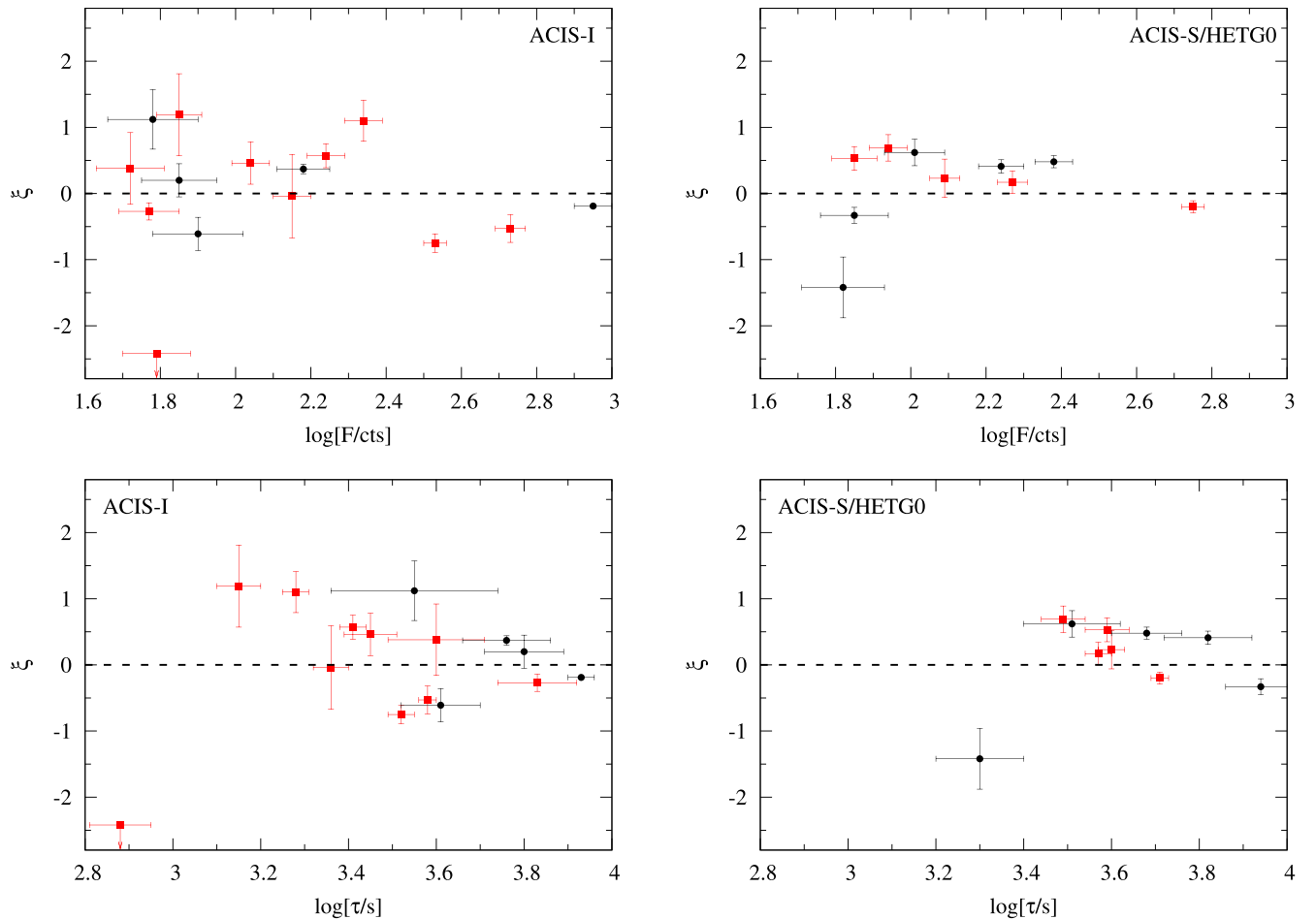


Figure 4. Top panels: the profile asymmetry parameter ξ versus the fluence for our detected flares with $F > 50$ cts in the ACIS-I (left) and -S/HETGO (right) samples. Bottom panels: ξ versus the duration of the same flares. Red squares are for isolate single flares, while black dots are for those with an apparent multiple subflare signature (see Paper I).

for an opposite example. The result obtained in this work slightly favours the former one.

Starting from a generic point of view, we may consider that the X-rays from a flare are predominantly generated via a single ra-

diative process. Collocated particles, presumably electrons, emit the polarized NIR/IR synchrotron radiation. As for the X-rays, bremsstrahlung (Liu & Melia 2002), inverse Compton scattering (Yuan et al. 2003; Eckart et al. 2004; Liu et al. 2006; Marrone

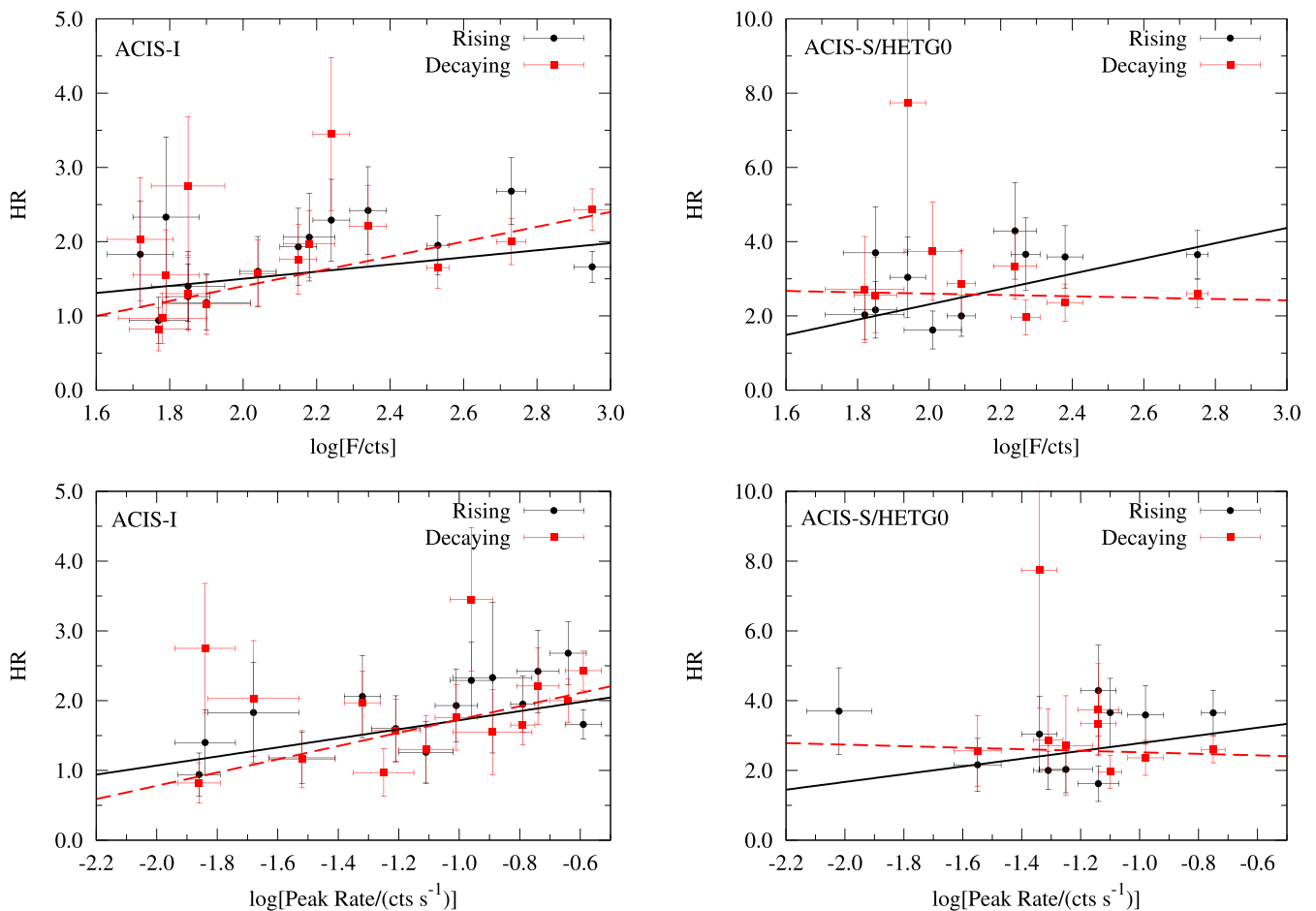


Figure 5. The HR versus the fluence (top panels) or peak rate (bottom panels) for the flares with $F > 50$ cts in the ACIS-I (left) and -S/HETGO (right) samples. Lines show the linear fits characterization of the correlation between the two parameters for the rising and decaying phases separately.

Table 4. The best-fitting values and 68 per cent uncertainties of the parameters characterizing the HR–fluence correlation $HR = \lambda \cdot \log F + \eta$.

	Rising		Decaying	
	λ	η	λ	η
ACIS-I	0.48 ± 0.24	0.54 ± 0.56	1.00 ± 0.24	-0.60 ± 0.55
ACIS-S/HETGO	2.06 ± 0.83	-1.81 ± 1.77	-0.18 ± 0.79	2.96 ± 1.90

Table 5. The best-fitting values and 68 per cent uncertainties of the parameters characterizing the HR–peak rate correlation $HR = \mu \cdot \log P + \nu$.

	Rising		Decaying	
	μ	ν	μ	ν
ACIS-I	0.65 ± 0.24	2.37 ± 0.29	0.95 ± 0.25	2.68 ± 0.29
ACIS-S/HETGO	1.11 ± 0.94	3.89 ± 1.16	-0.22 ± 1.03	2.30 ± 1.05

et al. 2008; Yusef-Zadeh et al. 2012) and synchrotron processes (Yuan, Quataert & Narayan 2003, 2004; Dodds-Eden et al. 2009; Ponti et al. 2017) have been suggested as processes which give rise to the temporal and spectral behaviours observed in Sgr A*.

The bremsstrahlung requires a large emission measure, and hence a high plasma density in the emission region. Although it is possible for a local pocket of high-density plasma (cf. plasmoids as in Yuan et al. 2009) to develop in an accretion inflow or outflow near the black hole through, for example radiatively induced instabili-

ties (see Liu & Melia 2002), certain fine tuning is required in such bremsstrahlung models in order to explain the X-ray flares. The X-rays can also be produced when low-energy photons in the ambient field are Compton up-scattered by the energetic electrons which emit the polarized NIR/IR flare emission. During the flaring events, the NIR/IR synchrotron photons dominate the radiation field in the vicinity of Sgr A*, and thus the X-rays are a consequence of self-Comptonization of the synchrotron radiation, i.e. a synchrotron self-Compton (SSC) scattering process. As the X-rays and the NIR radiation are assumed to originate from the same region, by combining the data obtained in the NIR and X-ray observations, one can constrain the effective source size and the particle density (Liu, Melia & Petrosian 2006; Dodds-Eden et al. 2009). An analysis of a simultaneous NIR to X-ray flare by Dodds-Eden et al. (2009) showed that the SSC model yielded very extreme conditions for the emission region: an extremely small linear size (of $\sim 0.001 - 0.1$ Schwarzschild radius), a very strong magnetic field (of $\sim 10^2 - 10^4$ G) and a very high particle density (of $\sim 10^8 - 10^{12}$ cm^{-3}). The SSC model is therefore unlikely if NIR and X-ray flares are generated in the same location.

Simultaneous observations of a very bright flare from NIR to X-ray revealed a spectral break between the NIR and X-ray spectra with a difference of the slopes $\Delta\Gamma = 0.57 \pm 0.09$ (Ponti et al. 2017). One may argue that this points to synchrotron radiation in the presence of radiative cooling. However, the result must be interpreted

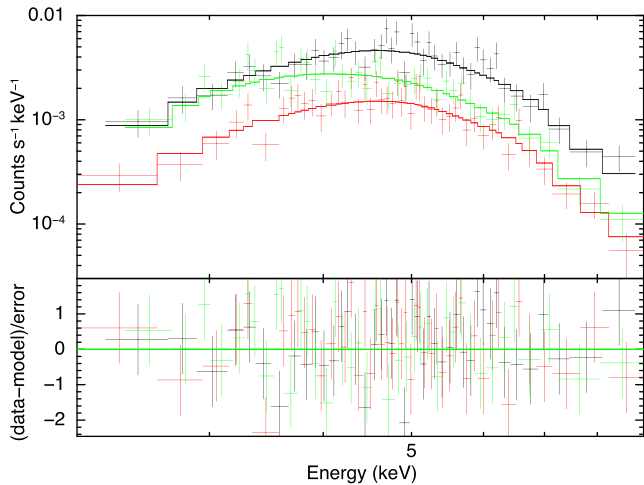


Figure 6. Left-hand panel: joint power-law model fit to the Sgr A* flare spectra. They are accumulated for the strong (black) and weak (red) flares detected with the XVP ACIS-S/HETGO data separately, as well as the flares detected with the ACIS-I data (green). The spectral contributions from the quiescent emission, estimated from the respective data, have been subtracted. Right-hand panel: 68, 90 and 99 percent confidence contours of the power-law photon index versus the absorption column density of the fit.

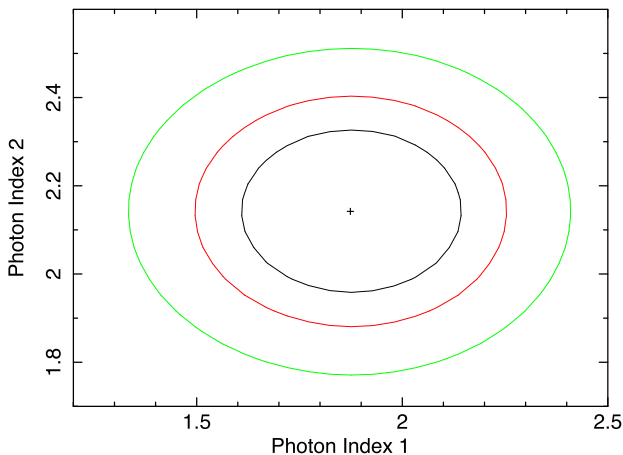
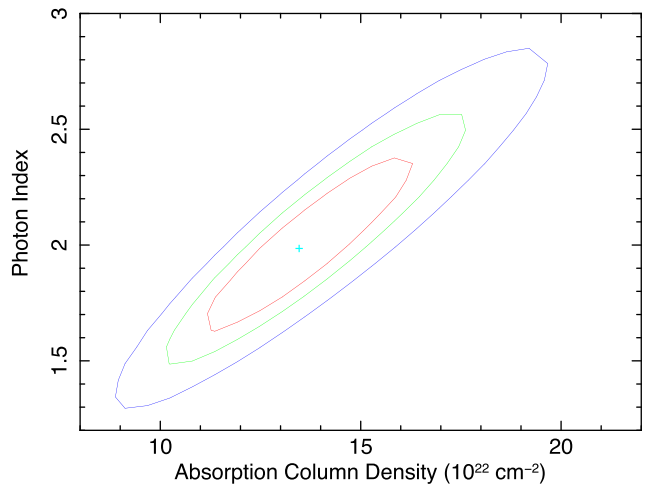


Figure 7. 68, 90 and 99 percent confidence contours of the two photon indices for the strong flares (1) and the weak ones (2).

with caution. If the NIR synchrotron flares are produced by the same population of electrons which are injected into the emission region as the X-ray ones and no efficient particle escape, we would expect a delay of NIR emission with respect to the X-ray one on the radiative cooling time-scale. The observations do not support such a delay (Ponti et al. 2017).

For a homogeneous emission region with a single instantaneous particle injection, the effective cooling time can be estimated from the observed peak of the radiative spectrum ν_m , as $\tau_{\text{cool}} = 5 \times 10^{11} (B \sin \alpha)^{-3/2} \nu_m^{-1/2}$ s (see Tucker 1975), where B is the magnetic field threading the region and α is the pitch angle of the electrons with respect to the magnetic field. If we assume that $B \sim 10$ G (Dodds-Eden et al. 2009) and the electron momentum distribution is isotropic, for $\nu_m \sim 10^{18}$ Hz we have $\tau_{\text{cool}} \sim 0.75$ min. As the cooling time is much shorter than the duration of a flare, the acceleration (or injection) of electrons therefore cannot be due to an impulsive single event. The flare’s variability is therefore caused by the dynamical evolution of the system, with temporal variations in the injection process, if a single emission region dominates.



Alternatively, spatial propagation of magnetic eruption fronts will lead to multiple injection/acceleration sites, giving rise to multiple emission regions.

Our analyses show no significant difference in the HRs between the rising and decaying phases (Fig. 5), which does not support the shutdown of the flare being due to synchrotron cooling in a uniform plasma, because of the short cooling time-scale and the anticipated dramatic spectral softening. Such persistence of the HR is however allowed, if the radiative particles escape from the region or the magnetic field dissipates. It is also allowed if the system is dynamical, with multiple particle injection/acceleration episodes and/or continuous particle injection/acceleration along a propagating magnetic reconnection front.

3.2 Origin of flares

We compare our improved statistical constraints on the fluence and duration distributions of the X-ray flares with the predictions of the various scenarios for the generation of Sgr A* X-ray flares. Among the broad class of magnetic reconnection scenarios for eruptive flares, SOC is a variant of the phenomenological models allowing a propagating front. The flare statistics in an SOC model depend on the effective geometric dimension of the system. For instance, a classical diffusion model predicts $\alpha_E = 3/2$ for the total energy (or the fluence) distribution, $\alpha_T = 2$ for the duration distribution and $\beta = 1/2$ for the duration–fluence correlation, for the spatial dimension of $S = 3$ (Aschwanden et al. 2016). The observations of solar flares give on average $\alpha_E = 1.62 \pm 0.12$ and $\alpha_T = 1.99 \pm 0.35$, which are well consistent with the SOC predictions with $S = 3$ (Aschwanden et al. 2016).

The (joint) statistical analysis of the X-ray flares in Section 2.1 reveals that the fluence distribution slope is $\alpha \sim 1.7$, with the 95 percent lower limit of 1.54, which is considerably larger than the prediction of the simple SOC model for $S = 3$. The duration versus fluence correlation is found to be very weak ($\beta \sim 0$). The 95 percent upper limit of β is about 0.23, which is substantially smaller than that (0.5) expected from the classical fractal diffusive SOC model. These results imply that the X-ray flares may not be

self-similar, as predicted by the simple SOC model. It is possible that the non-uniform scenario of the SOC model with, e.g. finite boundary conditions is responsible for such distributions of the flares. Alternatively, the X-ray fluence may not be a good measurement of the total energy of a flare.

A very different scenario for the production of Sgr A* flares is the tidal disruption of asteroids by the SMBH (e.g. Čadež, Calvani & Kostić 2008; Kostić et al. 2009; Zubovas, Nayakshin & Markoff 2012). Asteroids could be split into small pieces when passing close enough (e.g. within 1 au) by the SMBH. They may then be vaporized by bodily friction with the accretion flow. A transient population of high-energy particles may be produced via the shock due to the bulk kinetic energy of an asteroid and/or plasma instabilities, leading to a flare of radiation (Zubovas et al. 2012). This asteroid disruption and evaporation model explains the luminosities, time-scales and event rates of the flares, at least on the orders of magnitude. There is so far no clear prediction for the fluence distribution as well as the fluence–duration correlation of the model. However, in a very simple and rough analogy of the Galactic centre environment to the Oort cloud of the Solar system, one may assume that the size distribution of asteroids can be characterized by a power law, $dn(r)/dr \propto r^{-q}$, with $q \sim 3 - 4$ (Zubovas et al. 2012). The fluence distribution of the flares simply follows the mass function of asteroids, which is $dn/dM \propto M^{-(q-2)/3}$. Therefore, we have $\alpha \sim 1.7 - 2$, which is consistent with that obtained in our analysis (see Table 3). The typical duration of a flare is then determined by the fly-by time of the asteroid, which is independent of the asteroid size (Zubovas et al. 2012). The predictions of the model are thus consistent with our observations. More detailed modelling of the asteroid distribution in the Galactic centre environment, as well as the disruption and radiation processes of this scenario, is needed to further test its viability.

3.3 SMBH environment effect on the flare profile

Most of astronomical flaring events, such as the soft X-ray and lower energy emission from γ -ray bursts (GRBs; Fishman & Meegan 1995) and (low-energy) solar flares (Fletcher et al. 2011), show ‘fast rise and slow decay’ light curves (i.e. $\xi > 0$), revealing the fast acceleration and slow depletion (via e.g. cooling or escape; Li et al. 2017) of particles. Our analysis of the flare profiles of Sgr A* in Section 2.2 shows that almost half of the flares have such common ‘fast rise and slow decay’ light curves and the other half are opposite, which is analogous to the impulsive component of the hard X-rays and higher energy emission of solar flares and GRBs. This result may also indicate that the observed light curves are not intrinsic and may result from radiation propagation in the extreme environment of the SMBH. The general anticorrelation between ξ and $\log \tau$ as shown in Fig. 4 supports this picture. Intrinsically flares are most likely produced with shorter durations and ‘fast rise slow decay’ profiles. The observed broader and diverse light curves may largely result from the gravitational lensing and Doppler effects due to the orbital motion and/or the general relativity frame dragging. These effects tend to smear the light curve of a flare, giving less distinct sub-structures of its profile (Younsi & Wu 2015). The effects also depend on the flare starting position relative to the black hole and increase with the inclination angle of the accretion flow and with the spin of the SMBH. Furthermore, the effects are energy dependent, which may be used to distinguish them from the intrinsic properties of flares. Therefore, with sufficient counting statistics and energy coverage of observations, Sgr A* X-ray flares can, in principle, be used to probe the spin and the space–time structure

around the event horizon of the SMBH, as well as the inclination angle of the innermost accretion disc.

4 SUMMARY

We have studied the statistical properties of a sample of 82 flares detected in the *Chandra* observations from 1999 to 2012 (Paper I). In the analysis of the flare fluences and their correlation with the durations, we use the MCMC technique to forward fit model parameters, accounting for both detection incompleteness and bias, which are found to be very important. We further systematically analyse the light curve asymmetry and spectral HR of individual bright flares with fluences > 50 counts, as well as the accumulated spectra of relatively weak flares. We summarize our major findings as follows.

- (i) The fluence distribution can be well modelled by a power law with a slope of $1.73^{+0.20}_{-0.19}$, which is inconsistent with the prediction of 1.5 from the simple classical fractal diffusive SOC model with a geometric dimension $S \lesssim 3$.
- (ii) There is no statistically significant correlation between the flare fluence and duration, which is again inconsistent with the prediction of the simple SOC model. The intrinsic duration dispersion of the flare is about 0.3 dex around the best-fitting power-law relation.
- (iii) About half of the relatively bright flares show ‘fast rise and slow decay’ profiles, whereas the other half are opposite. This is different from the commonly observed ‘fast rise and slow decay’ profiles from astrophysical transients, such as GRBs and solar flares, indicating that the flare shape may not be intrinsic. The gravitational lensing and Doppler effects of the flare radiation around the SMBH may play a dominant role in regulating the shape.
- (iv) The accumulated spectra of the flares can be well characterized by a power law of photon index $\Gamma = 2.0 \pm 0.4$. We find a marginal trend that the spectra of brighter flares are harder than those of relatively weak ones. No significant HR difference between the rising and decaying phases of the X-ray flares is found.

While these results provide new constraints on the origin of Sgr A* flares, as well as their X-ray emission mechanism, more detailed modelling of their production and evolution is clearly needed. In particular, dedicated simulations of photons travelling through the space and time, strongly affected by the presence of the SMBH and the resulting flare shapes, will be useful for a comparison with the observations. Such a comparison will provide important tests on various scenarios for the production of the X-ray flares and a potential tool to measure the spin of the SMBH.

ACKNOWLEDGEMENTS

We thank the referee for constructive comments, which helped to improve the presentation of the paper. QY is supported by the 100 Talents program of Chinese Academy of Sciences. QDW acknowledges the support of NASA via the SAO/CXC grant G06-17024X.

REFERENCES

- Aschwanden M. J., 2011, *Sol. Phys.*, 274, 99
 Aschwanden M. J., 2012, *A&A*, 539, A2
 Aschwanden M. J. et al., 2016, *Space Sci. Rev.*, 198, 47
 Baganoff F. K. et al., 2001, *Nature*, 413, 45
 Baganoff F. K. et al., 2003, *ApJ*, 591, 891
 Bak P., Tang C., Wiesenfeld K., 1987, *Phys. Rev. Lett.*, 59, 381

- Barrière N. M. et al., 2014, *ApJ*, 786, 46
 Bélanger G., Goldwurm A., Melia F., Ferrando P., Grosso N., Porquet D., Warwick R., Yusef-Zadeh F., 2005, *ApJ*, 635, 1095
 Čadež A., Calvani M., Kostić U., 2008, *A&A*, 487, 527
 Cash W., 1979, *ApJ*, 228, 939
 Davis J. E., 2001, *ApJ*, 562, 575
 Degenaar N., Miller J. M., Kennea J., Gehrels N., Reynolds M. T., Wijnands R., 2013, *ApJ*, 769, 155
 Dodds-Eden K. et al., 2009, *ApJ*, 698, 676
 Eckart A. et al., 2004, *A&A*, 427, 1
 Eckart A. et al., 2006, *A&A*, 450, 535
 Fishman G. J., Meegan C. A., 1995, *ARA&A*, 33, 415
 Fletcher L. et al., 2011, *Space Sci. Rev.*, 159, 19
 Genzel R., Schödel R., Ott T., Eckart A., Alexander T., Lacombe F., Rouan D., Aschenbach B., 2003, *Nature*, 425, 934
 Katz J. I., 1986, *J. Geophys. Res.*, 91, 10412
 Kennea J. A. et al., 2013, *ApJ*, 770, L24
 Kostić U., Čadež A., Calvani M., Gomboc A., 2009, *A&A*, 496, 307
 Li Y.-P., Yuan F., Wang Q. D., 2017, *MNRAS*, 468, 2552
 Li Y.-P. et al., 2015, *ApJ*, 810, 19
 Liu S., Melia F., 2002, *ApJ*, 566, L77
 Liu S., Melia F., Petrosian V., 2006, *ApJ*, 636, 798
 Liu S., Petrosian V., Melia F., Fryer C. L., 2006, *ApJ*, 648, 1020
 Lu E. T., Hamilton R. J., 1991, *ApJ*, 380, L89
 Marrone D. P. et al., 2008, *ApJ*, 682, 373
 Mossoux E., Grosso N., 2017, *A&A*, 604, A85
 Narayan R., Śądowski A., Penna R. F., Kulkarni A. K., 2012, *MNRAS*, 426, 3241
 Neilsen J. et al., 2013, *ApJ*, 774, 42
 Nowak M. A. et al., 2012, *ApJ*, 759, 95
 Ponti G. et al., 2015, *MNRAS*, 454, 1525
 Ponti G. et al., 2017, *MNRAS*, 468, 2447
 Porquet D., Predehl P., Aschenbach B., Grosso N., Goldwurm A., Goldoni P., Warwick R. S., Decourchelle A., 2003, *A&A*, 407, L17
 Porquet D. et al., 2008, *A&A*, 488, 549
 Roberts S. R., Jiang Y.-F., Wang Q. D., Ostriker J. P., 2017, *MNRAS*, 466, 1477
 Smith R. K., Valencic L. A., Corrales L., 2016, *ApJ*, 818, 143
 Stancik A., Brauns E., 2008, *Vib. Spectrosc.*, 47, 66
 Tucker W., 1975, *Radiation Processes in Astrophysics*. MIT Press, Cambridge, MA, USA
 Wang F. Y., Dai Z. G., 2013, *Nature Phys.*, 9, 465
 Wang Q. D. et al., 2013, *Science*, 341, 981
 Wang F. Y., Dai Z. G., Yi S. X., Xi S. Q., 2015, *ApJS*, 216, 8
 Wilms J., Allen A., McCray R., 2000, *ApJ*, 542, 914
 Younsi Z., Wu K., 2015, *MNRAS*, 454, 3283
 Yuan Q., Wang Q. D., 2016, *MNRAS*, 456, 1438
 Yuan F., Quataert E., Narayan R., 2003, *ApJ*, 598, 301
 Yuan F., Quataert E., Narayan R., 2004, *ApJ*, 606, 894
 Yuan F., Lin J., Wu K., Ho L. C., 2009, *MNRAS*, 395, 2183
 Yuan F., Gan Z., Narayan R., Sądowski A., Bu D., Bai X.-N., 2015, *ApJ*, 804, 101
 Yusef-Zadeh F. et al., 2006, *ApJ*, 644, 198
 Yusef-Zadeh F. et al., 2012, *AJ*, 144, 1
 Zhang S. et al., 2017, *ApJ*, 843, 96
 Zubovas K., Nayakshin S., Markoff S., 2012, *MNRAS*, 421, 1315

This paper has been typeset from a $\text{\TeX}/\text{\LaTeX}$ file prepared by the author.